Carbohydrate Polymers 255 (2021) 117328

Contents lists available at ScienceDirect

Carbohydrate Polymers

journal homepage: www.elsevier.com/locate/carbpol

Shear-induced unidirectional deposition of bacterial cellulose microfibrils using rising bubble stream cultivation

Inseok Chae [a,1], Syed M.Q. Bokhari [b,1], Xing Chen [c], Rui Zu [d], Ke Liu [b], Ali Borhan [a], Venkatraman Gopalan [d,e], Jeffrey M. Catchmark [b], Seong H. Kim [a,*]

[a] Department of Chemical Engineering, Pennsylvania State University, University Park, PA 16802, United States
[b] Department of Agricultural and Biological Engineering, Pennsylvania State University, University Park, PA 16802, United States
[c] Department of Chemistry, Pennsylvania State University, University Park, PA 16802, United States
[d] Department of Materials Science and Engineering, Pennsylvania State University, University Park, PA 16802, United States
[e] Department of Physics, Pennsylvania State University, University Park, PA 16802, United States

ARTICLE INFO

Keywords:
Bacterial cellulose microfibrils
Bubble stream
Shear stress
Polar alignment
Sum frequency generation

ABSTRACT

In crystalline cellulose I, all glucan chains are ordered from reducing ends to non-reducing ends. Thus, the polarity of individual chains is added forming a large dipole within the crystal. If one can engineer unidirectional alignment (parallel packing) of cellulose crystals, then it might be possible to utilize the material properties originating from polar crystalline structures. However, most post-synthesis manipulation methods reported so far can only achieve the uniaxial alignment with bi-directionality (antiparallel packing). Here, we report a method to induce the parallel packing of bacterial cellulose microfibrils by applying unidirectional shear stress during the synthesis and deposition through the rising bubble stream in a culture medium. Driving force for the alignment is explained with mathematical estimation of the shear stress. Evidences of the parallel alignment of crystalline cellulose Iα domains were obtained using nonlinear optical spectroscopy techniques.

1. Introduction

Structural ordering of biologically produced materials is an essential task in biomanufacturing as it enables us to characterize and utilize the material properties intrinsic to the unique structures that living organisms can synthesize (Chae, Jeong, Ounaies, & Kim, 2018, 2020; Chung et al., 2011; Lee JH et al., 2017; Yao, Meng, Bulone, & Zhou, 2017). In many biopolymers such as cellulose, chitin, and collagen, the polymer chains are directionally produced by synthase complexes in cell wall membranes, then assembled into crystalline phases (Ogawa et al., 2013; Koyama, Helbert, Imai, Sugiyama, & Henrissat, 1997; Lai-Kee-Him et al., 2002; Shoulders & Raines, 2009). For instance, cellulose microfibrils are produced by the cellulose synthase complex (CSC) through sequential unidirectional additions of the reducing ends of individual glucose monomeric units to non-reducing end of cellulose chain. The resulting β-1,4-glucan chains are extruded from the CSC and assembled into non-centrosymmetric crystalline microfibrils (Kim, Imai, Wada, & Sugiyama, 2006; Koyama et al., 1997; Morgan, Strumillo, & Zimmer, 2013; Morgan, McNamara, & Zimmer, 2014; Morgan et al., 2016). Due to the directional packing of cellulose chains, a large dipole has been anticipated within the crystal (Frka-Petesic, Jean, & Heux, 2014). Also, anisotropic properties, such as piezoelectricity, unique to asymmetric crystal structures are expected for such crystalline cellulose (Chae et al., 2020; Chang et al., 2015; Cranston & Gray, 2008; Diddens, Murphy, Krisch, & Müller, 2008; Frka-Petesic et al., 2014; Frka-Petesic, Sugiyama, Kimura, Chanzy, & Maret, 2015; Iyer, Neelakantan, & Radhakrishnan, 1968). The anisotropic properties of crystalline domains, typically in nanoscale, can appear in a macroscopic sample if such domains are preferentially aligned such that the asymmetric properties of adjacent domains add up to a macroscopic domain rather than cancelling each other (Chae et al., 2018).

Numerous *post-synthesis* alignment approaches have been explored to induce the macroscopic arrangement of crystalline cellulose and utilize their unique properties (Chae et al., 2020; Dumanli et al., 2014; Lagerwall et al., 2014). Typically, an external force from mechanical shear or stretching, electric field, or magnetic field was applied to isolated

* Corresponding author.
E-mail addresses: ibc5029@psu.edu (I. Chae), sub873@psu.edu (S.M.Q. Bokhari), xzc4@psu.edu (X. Chen), ruz147@psu.edu (R. Zu), kvl5318@psu.edu (K. Liu), axb20@psu.edu (A. Borhan), vgopalan@psu.edu (V. Gopalan), jmc102@psu.edu (J.M. Catchmark), shkim@engr.psu.edu, shk10@psu.edu (S.H. Kim).
[1] These authors contributed equally to this work.

https://doi.org/10.1016/j.carbpol.2020.117328
Received 31 August 2020; Received in revised form 24 October 2020; Accepted 25 October 2020
Available online 3 November 2020

crystals interspersed in a media where they can rotate and translate (Bordel, Putaux, & Heux, 2006; Chae, Ngo, Makarem, Ounaies, & Kim, 2019; Chang et al., 2015; Gindl, Emsenhuber, Maier, & Keckes, 2009; Hoeger, Rojas, Efimenko, Velev, & Kelley, 2011; Huang, Wang, & Yan, 2010). Under the external force or field, they can be aligned into ordered phases such as nematic or chiral nematic phase (Barhoumi Meddeb, Chae, Han, Kim, & Ounaies, 2020; Bordel et al., 2006; Chae et al., 2019; Csoka, Hoeger, Peralta, Peszlen, & Rojas, 2011; De France, Yager, Hoare, & Cranston, 2016). Recently, new approaches have been reported to induce the structural ordering of crystalline cellulose by applying directional force or field *during the synthesis* (Putra, Kakugo, Furukawa, Gong, & Osada, 2008; Sano, Rojas, Gatenholm, & Davalos, 2010; Wan et al., 2015; Zang et al., 2014). It was speculated that the external force or field moves bacteria, which synthesize crystalline cellulose, along a certain direction during the synthesis (Putra et al., 2008; Sano et al., 2010; Wan et al., 2015). The aligned cellulose microfibrils showed anisotropic optical and mechanical properties (Sano et al., 2010; Wan et al., 2015; Zang et al., 2014).

The parallel directionality of crystalline cellulose, i.e., the same polarity or uni-directionality along the preferential alignment direction, is a prerequisite to utilize piezoelectricity and pyroelectricity originating from the noncentrosymmetry of the nanocrystalline domains (Chae et al., 2018; García, Ruiz-Blanco, Marrero-Ponce, & Sotomayor-Torres, 2016; Halasyamani & Poeppelmeier, 1998; Rajala et al., 2016). In random or anti-parallel alignment (equally probable alignment along two opposite directions or bi-directional without any bias along one direction over the other), these properties would be negligible or insignificant because individual responses of neighboring crystals aligned along two opposite directions would be cancelled (Chae et al., 2018; Trolier-McKinstry, 2008). It has been challenging to induce the parallel packing of cellulose crystals from an isotropic phase (such as crystals randomly dispersed in solution) because the random orientations along the alignment direction (which is equivalent to the anti-parallel packing in average) are entropically more favorable than the parallel packing (Chae et al., 2018). Many naturally-produced cellulose-containing materials have the anti-parallel packing of crystalline domains on average over the macroscopic length scale (Chae et al., 2018; Lee, Kafle, Park, & Kim, 2014). Chemical modifications are possible to selectively tag nanoparticles on the reducing ends of cellulose crystals (Arcot, Lundahl, Rojas, & Laine, 2014; Hieta, Kuga, & Usuda, 1984; Kim et al., 2006; Koyama et al., 1997; Lai-Kee-Him et al., 2002; Lokanathan et al., 2013). However, the methods are limited to isolated individual units and it is still challenging to deposit multiple layers of ordered cellulose crystals with the parallel alignments using such methods.

For the symmetry-driven material property study, it is also critical to distinguish the parallel packing from anti-parallel or random packing. It is difficult to distinguish the polarity of the cellulose crystals through high-resolution electron microscopy because they look symmetric topographically. Conventional spectroscopic techniques such as infrared (IR), Raman, or nuclear magnetic resonance (NMR) cannot distinguish the two cases either, because they are not sensitive to the polarity of molecules (Kim, Lee, & Kafle, 2013). Nonlinear optical techniques such as sum frequency generation (SFG) spectroscopy and second harmonic generation (SHG) can be a very useful technique for this task because they are sensitive only to non-centrosymmetric components in the medium (Chae et al., 2019; Denev, Lummen, Barnes, Kumar, & Gopalan, 2011; Lee, Chen, Weiss, Jensen, & Kim, 2017). Within the coherence length of SFG or SHG detection, the signals are added for parallel packing, but cancelled for anti-parallel packing (Denev et al., 2011; Lambert, Davies, & Neivandt, 2005; Lee et al., 2014; Makarem et al., 2019). This noncentrosymmetry requirement makes SFG and SHG an excellent platform to test the polarity of non-centrosymmetric crystals (Chae et al., 2017, 2019; Denev et al., 2011; Makarem et al., 2019).

We developed a new method to induce the parallel packing of bacterial cellulose microfibrils (BCMs) on a macroscopic scale and confirmed the added polarity of crystalline domains. The parallel packing of BCMs was achieved by applying unidirectional shear stress to the bacteria during the culture through the rising bubble stream in a culture medium. *Gluconacetobacter hansenii* (*G. hansenii,* ATCC 23769) bacterial strain was employed in this study as it produces cellulose Iα crystals (with a minor fraction of cellulose Iβ) substantially in a few days (Kondo et al., 2002; Koyama et al., 1997; Lee, Gu, Kafle, Catchmark, & Kim, 2015). A cylindrical BCM tube with the parallel packing of cellulose Iα crystals along the chain axis was formed at the periphery of the bubble stream in the culture medium. Direct evidence of the parallel packing was obtained through the comparison of experimentally measured SFG signals with time-dependent density functional theory (TD-DFT) calculations of nonlinear susceptibility ($\chi_{eff}^{(2)}$). Besides, the parallel-aligned BCM tube generated a strong SHG signal as the polarity of cellulose crystalline domains were added by the parallel packing.

2. Materials and methods

2.1. Preparation of bacterial strain and culture medium

Bacterial strain *G. hansenii* was obtained from the American Type Culture Collection (ATCC). The cultivation of this bacteria was performed in the standard Hestrin-Schramm (HS) medium containing 20.0 g of D-(+)-glucose (Fluka Analytical, Sigma Aldrich, USA), 5.0 g of Bacto Peptone (Becton, Dickinson and Co., USA), 5.0 g of Bacto yeast extract (Becton, Dickinson and Co., USA), 2.7 g of sodium phosphate dibasic anhydrous (Fisher Chemical, USA), 1.15 g of citric acid (Fluka Analytical, Sigma Aldrich, USA) and 1.0 g of magnesium sulfate (General, BDH, USA) per liter of ultra-pure water with a resistivity of 18.2 MΩ/cm (Millipore Milli-Q UF Plus) (Hestrin & Schramm, 1954; Liu & Catchmark, 2019). The pH of this culture medium was adjusted to 5.0 by adding 4 M hydrochloric acid.

2.2. Cultivation of BCM with bubble stream

The cultivation vessel was designed to produce aligned BCM at the air bubble-liquid interface, as shown in Fig. 1. A 50 mL centrifuge tube (VWR, USA) was used as the cultivation vessel with two holes drilled out in the cap. An L-shaped silicone (polydimethylsiloxane) tube (Vanguard 70 Duro, McMaster-Carr, USA) with an inner diameter of 3 mm and an outer diameter of 5 mm was inserted through the cap, then positioned at the bottom of the vessel. The bubbling path was created by puncturing a pinhole with a diameter of 0.45 mm in the center of the silicone tube facing upwards, as shown in Fig. 1. This pinhole size was determined to be an optimum for the given size of the cultivation vessel and the flow rate after preliminary testing of the BCM tube formation with different sizes of holes varying from 0.45 mm to 6 mm. The vessel and silicone tube were washed with soap water, air dried, then sprayed with 70 % (v/v) ethanol (VWR, USA), then sterilized with UV for 30 min in the biosafety cabinet before use. A sterile environment was maintained in the cultivation vessel by placing two 0.22 μm filters (VWR, USA) at the inlet and outlet of the air source.

For the cultivation of bacterial cellulose under the bubble stream, a 1 % (v/v) primary culture of ATCC 23769 was inoculated into the cultivation vessel containing 30 mL culture media. The cultivation was performed in the incubator at 30 °C for three days. After three days, BCM pellicles started forming at the top air/solution interface, so the culture duration was kept at three days in this study. The supply rate of compressed wet air through the silicone tube was set as 0.25 vvm [air volume flow (liter) per unit of liquid volume (liter) per minute (min)], during the entire cultivation period. The wet air was used to minimize media evaporation during the cultivation period. The bubble stream was generated by a flow of wet compressed air passing through the small pinhole in the silicone tube. After the cultivation, the BCM tube was collected, then rinsed with plenty of ultra-pure water. The washed BCM

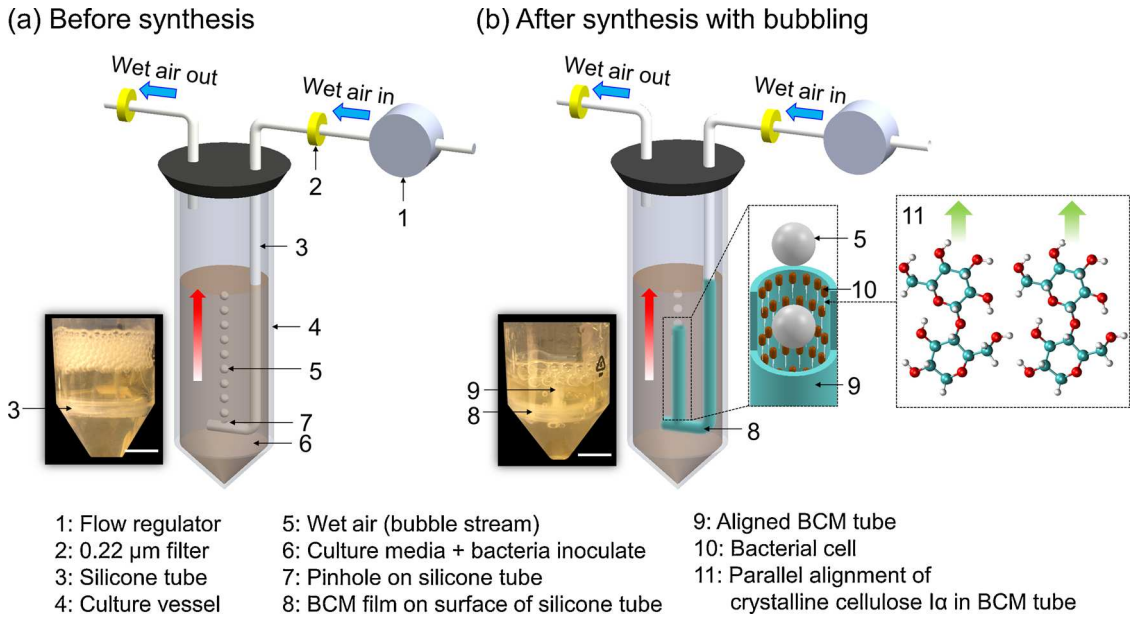

Fig. 1. Schematics of the bubble stream-induced parallel alignment of BCMs during the synthesis in the cultivation vessel. (a) Before the cultivation and (b) after the cultivation at 30 °C for three days. The white scale bars in photographic images represent 1 cm. The red arrows represent the direction of rising bubbles. The sky blue, red, and grey color balls of cellulose Iα represent C, O, and H, respectively. The green arrows represent the expected direction of bacterial movement due to the bubble stream.

tube was soaked in 1% (w/v) sodium hydroxide solution, then sterilized in the autoclave at 121 °C for 20 min to remove the bacterial cell debris and alkali-soluble components. The solution was cooled at room temperature, followed by rinsing with ultra-pure water until pH 7.0 was achieved. The BCM tube was stored in a swollen state in ultra-pure water at 4 °C. The purified BCM tube was frozen at −80 °C overnight (Laboratory Freezer ULT2186, Thermo Fisher Scientific, USA), freeze-dried (Freezone 2.5 L, Labconco, USA) for 24 h, then stored in a desiccator for the further analyses.

2.3. Field-Emission scanning electron microscopy (SEM)

Field-emission SEM (Zeiss SIGMA VP-FESEM, Thornwood, NY) was used to investigate the alignment of bacterial cellulose microfibrils. 5 nm of iridium was coated on the dried sample using a Leica EM ACE600 sputter coater (Leica, Wetzlar, Germany), then the sample was mounted onto aluminum stub using carbon tape. An accelerating voltage of 3 keV with a working distance of 4 mm was used for the imaging.

2.4. Wide-angle X-ray scattering (WAXS)

Two-dimensional (2D) X-ray scattering in a transmission mode was performed using the in-house WAXS system (Xeuss 2.0 HR, Xenocs, France) equipped with X-ray wavelength of 1.54 Å (50 kV, 0.6 mA) and Pilatus3 R200 K detector with the sample-to-detector distance of ~0.165 m.

2.5. Vibrational SFG spectroscopy

The femtosecond broadband SFG system was used to identify the parallel alignment of BCMs. A narrow band of 800 nm pulse was produced by spectral filtering of the fundamental output of the Ti-sapphire amplifier. A broadband IR pulse (half maximum of ~160 cm^{-1}) with a center wavenumber of 2900 cm^{-1} and 3340 cm^{-1} was used to detect C—H and O—H modes, respectively. The 800 nm and mid-IR pulse were focused onto the bacterial cellulose microfibrils with the incident angle of 45°. The generated SFG in a reflection mode was filtered using a short-pass filter and monochromator, then detected using a CCD camera. The SFG peak intensities of C—H and O—H modes as a function of azimuth angle were obtained by rotating the sample on the stage from 0° to 360° with 10° per step using the motorized rotation mount (KPRM1E, Thorlabs).

2.6. TD-DFT calculation of SFG

The cellulose Iα chains in a single crystalline domain were represented by four dimeric units, perpendicularly stacking with respect to the chain direction. All theoretical simulations were performed using the NWChem package (Valiev et al., 2010). Under the Placzek approximation, the hyperpolarizability is related to the product of polarizability and dipole derivatives,

$$\beta_{abc}(\omega_{SFG},\omega_{VIS},\omega_{IR}) = \sum_{q}\frac{-\hbar}{2\omega_q}\frac{\partial\alpha_{ab}}{\partial Q_q}\frac{\partial\mu_c}{\partial Q_q}\left(\frac{1}{\omega_{IR}-\omega_q+\Gamma_q}\right) \quad (1)$$

where ω_{SFG}, ω_{VIS}, and ω_{IR} are the frequencies of SFG signal, visible, and IR input photons. The transition lifetime (Γ_q) was set to 10 cm^{-1}. The molecular frame (c, b, a) transforms into the laboratory coordinates (X, Y, Z) through the Euler rotation (R) matrix. In this way, the chain axis (c-axis in the molecular frame) aligns with the X-axis of the laboratory frame. The second-order susceptibility tensor ($\chi^{(2)}_{XYZ}$) is represented as:

$$\chi^{(2)}_{XYZ} = N\sum_{cba}\langle R_{Xc}R_{Yb}R_{Za}\rangle\beta_{cba} \quad (2)$$

where N is the number density of the SFG-active moieties. At a given azimuth angle (ϕ), the SFG intensity of randomly orientated domains with respect to the uniaxial alignment axis can be written as:

$$I(\phi) = \frac{1}{n}\sum_{\theta}^{360^\circ}\chi_\theta(\phi)\chi^*_\theta(\phi) \quad (3)$$

Here, the rotation angle (θ) along the chain axis is sampled from 0° to 360° with an interval of 5°, and n is the total number of orientations. In this way, all probable orientations are treated equally. The effective $\chi^{(2)}$ with *spp*-(*s*-polarized SFG, *p*-polarized 800 nm, *p*-polarized IR) and *psp*-polarization combinations, as shown below, are plotted as a function of

ϕ in Fig. 3. For simplicity, the frequency-dependent Fresnel factors are set to 1.

$$\chi^{(2)}_{eff,\,spp} = \chi^{(2)}_{YXX} + \chi^{(2)}_{YZZ} + \chi^{(2)}_{YXZ} + \chi^{(2)}_{YZX} \tag{4}$$

$$\chi^{(2)}_{eff,\,psp} = (\chi^{(2)}_{ZYX} + \chi^{(2)}_{ZYZ}) - (\chi^{(2)}_{XYX} + \chi^{(2)}_{XYZ}) \tag{5}$$

The SFG intensity (I_{SFG}) for the parallel case at a certain azimuth angle (ϕ_*) is written as,

$$I_{SFG,\phi_*} \propto {\chi^{(2)}_{eff,\,spp,\,\phi_*}}^2 = (\chi^{(2)}_{YXX,\phi_*} + \chi^{(2)}_{YZZ,\phi_*} + \chi^{(2)}_{YXZ,\phi_*} + \chi^{(2)}_{YZX,\phi_*})^2 \tag{6a}$$

$$I_{SFG,\phi_*} \propto {\chi^{(2)}_{eff,\,psp,\,\phi_*}}^2 = (\chi^{(2)}_{ZYX,\,\phi_*} + \chi^{(2)}_{ZYZ,\phi_*} - \chi^{(2)}_{XYX,\phi_*} + \chi^{(2)}_{XYZ,\phi_*})^2 \tag{6b}$$

On the other hand, the SFG intensity for two domains that are anti-parallel to each other but separated farther than the coherence length is described as,

$$I_{SFG,\phi_*} \propto {\chi^{(2)}_{eff,\,spp,\,\phi_*}}^2 = \frac{1}{2}\cdot(\chi^{(2)}_{YXX,\phi_*} + \chi^{(2)}_{YZZ,\phi_*} + \chi^{(2)}_{YXZ,\phi_*} + \chi^{(2)}_{YZX,\phi_*})^2 + \frac{1}{2}\cdot(\chi^{(2)}_{YXX,\phi_*+\pi} + \chi^{(2)}_{YZZ,\phi_*+\pi} + \chi^{(2)}_{YXZ,\phi_*+\pi} + \chi^{(2)}_{YZX,\phi_*+\pi})^2 \tag{7a}$$

$$I_{SFG,\phi_*} \propto {\chi^{(2)}_{eff,\,psp,\,\phi_*}}^2 = \frac{1}{2}\cdot(\chi^{(2)}_{ZYX,\,\phi_*} + \chi^{(2)}_{ZYZ,\phi_*} - \chi^{(2)}_{XYX,\phi_*} + \chi^{(2)}_{XYZ,\phi_*})^2 + \frac{1}{2}\cdot(\chi^{(2)}_{ZYX,\,\phi_*+\pi} + \chi^{(2)}_{ZYZ,\phi_*+\pi} - \chi^{(2)}_{XYX,\phi_*+\pi} + \chi^{(2)}_{XYZ,\phi_*+\pi})^2 \tag{7b}$$

Additional details are available in Fig. S1 and Table S1 in Supporting Information.

2.7. SHG measurement

SHG measurement was performed in the normal transmission geometry. The incident beam was generated by the Ti: Sapphire femtosecond laser system ($\lambda = 800\,nm$, a repetition rate of 1 kHz), then propagated along the *Z*-axis in Fig. 5a (normal to the surface of BCM film). The aligned BCM film was placed on the sample stage as its parallel alignment (direction of rising bubble-stream) was along the *X*-axis. The SH responses with a fixed polarization parallel to *X*- and *Y*-axis were collected by rotating the incident polarization angle.

3. Results and discussion

3.1. Cultivation of aligned BCM tube with a bubbling

The cultivation vessel was designed to produce BCMs along one direction with the bubble stream. *G. hansenii* is an aerobic microorganism, which produces BCM using glucose in an oxygen-rich environment (Liu & Catchmark, 2019). Fig. 1 shows the schematics of the cultivation of bacterial cellulose with the rising bubble stream. The bubbles are rising through the culture medium from the pinhole of the silicone tube to the top air/liquid interface by the buoyancy force. Initially, bacterial cells produce BCMs on the surface of the silicone tube since it is oxygen permeable. Once the BCM film fully covers the silicone tube (8 in Fig. 1b), further growth is not sustained due to limited oxygen supply. On the other hand, bacterial cells near the pinhole of the silicone tube can continue to flourish because the fresh air is continuously supplied (7 in Fig. 1a). Subsequently, the vertical bubble stream pulls the bacterial cells contained in the growing BCM film upwards. The BCM film on the silicone tube near the pinhole acts as an anchoring site for the newly produced BCM tube (9 in Fig. 1b) along the bubble stream.

The cellulose microfibrils from bacterial cells are anchored or entangled in the BCM film at the silicone tube surface and the bacterial cells are pulled upwards by the shear stress from the rising bubbles. Thus, the free-standing BCM tube can grow upward from the pinhole. The vertical flow of the bubble stream continuously applies the upward shear force on anchored bacterial cells on the BCM tube. As bacterial cells continue to divide, they are tethered to the BCM film by the entanglement of BCMs. The bacterial cells remain near the bubble stream as they produce BCMs while tethered.

The flow rate of 0.25 vvm was the optimal flow rate to form and align the BCM tube; it was observed that if the flow was too slow or too fast, there was no growth of the BCM tube. In the case of flow being too slow, there might not be enough supply of oxygen to maintain BC synthesis near the pinhole. In the case of flow being too fast, the shear force might have been too strong so that cells were detached from the BCM film (Nejadnik, van der Mei, Busscher, & Norde, 2008). Because BCMs are continually produced by the bacteria during cell division, newly synthesized BCMs from both daughter and parent cells remain attached to the BCMs produced by the parent cell that is already integrated with the existing BCM tube. The bacterial cells are expected to be pushed upward by the rising bubbles, leaving the synthesized BCMs behind (Kondo et al., 2002). A layer of BCMs is produced at the bubble/liquid interface, and when the layer becomes saturated, new bacteria positioned at the inner side of the BCM tube can push the already formed layer into the culture medium (Bodin et al., 2007). Due to this layered formation, the vertical bubble stream can effectively apply the force upward on the newly synthesizing bacterial cells on the BCM tube.

The vertical alignment of the BCM along the rising bubble stream was confirmed by the SEM and XRD measurements, as shown in Fig. 2. The SEM image in Fig. 2(II) shows the uniaxially aligned BCMs. The 2D-WAXS pattern of aligned BCM tube with bubbling in Fig. 2(III) confirms the uniaxial alignment of BCM along the bubble stream axis. The diffraction peaks of (110), (010), and (100) of crystalline cellulose Iα are seen at the equator, meaning that the long axis of cellulose Iα (chain axis) is aligned along the bubble stream. For comparison, the control sample of BCM film was fabricated in a static environment without bubbling. The control sample shows the random arrangement of BCM in the SEM image [Fig. 2(IV)] and rings with uniform intensities along with all directions in the 2D-WAXS pattern [Fig. 2(V)]. The aligned BCMs in Fig. 2(II) look much thicker than the random BCMs in Fig. 2(IV) because aligned fibers can bundle together while randomly entangled fibers cannot. The thickness of the BCM tube was measured to be ~20 μm in a freeze-dried state.

3.2. Mathematical estimation of bubble size and shear stress

The bubble size and shear stress play the key roles in aligning BCMs in the produced tube. Since BCM is produced at the bubble/liquid interface, the size of the BCM tube is expected to be comparable to the size of air bubbles produced by the pinhole in the silicone tube. The spherical-equivalent diameter (d) of a bubble, that is ejected from the pinhole and moves up with velocity (U), can be estimated by considering the momentum balance on the bubble at the point of detachment (Ramakrishnan, Kumar, & Kuloor, 1969). Assuming the center of the growing bubble to be about the bubble diameter away from the pinhole at the time of detachment $t_d \sim \pi d^3/6\dot{V}_g$ (where $\dot{V}_g$ is the airflow rate), the bubble velocity and acceleration can be approximated as $U \sim d/t_d \sim 6\dot{V}_g/\pi d^2$ and $\dot{U} \sim U/t_d \sim 36\dot{V}_g^2/\pi^2 d^5$. Based on these scales, the inertial and drag forces on the bubble are negligibly small for the 0.25 vvm air flow rate used in the experiments. The bubble size can therefore be estimated from a dominant balance between the buoyancy force $\frac{\pi}{6}d^3(\rho - \rho_g)g$ and the surface tension force $\pi d_c \sigma\, sin\theta$ at the contact line, namely

$$d \sim \left(\frac{6d_c\sigma\, sin\theta}{\rho g}\right)^{1/3} \tag{8}$$

where ρ and ρ_g denote the densities of water and air, respectively. σ is

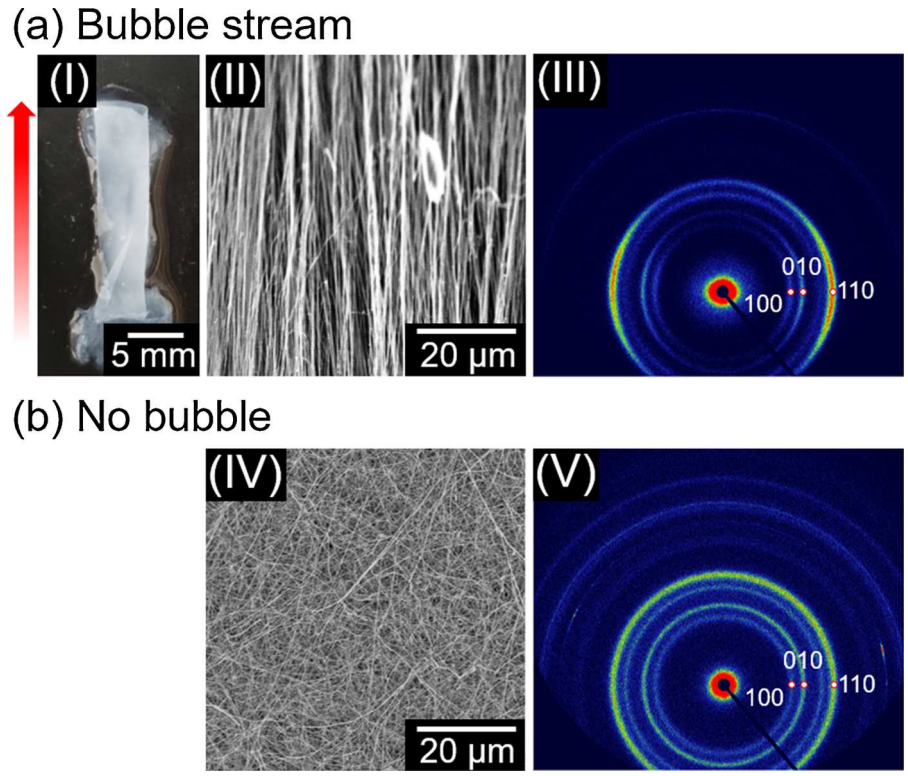

Fig. 2. Comparison of the alignment of BCM (a) with and (b) without bubble-stream. (I) Photographic image of BCM tube grown under the rising bubble stream. SEM and 2D-WAXS images of BCM grown (II, III) under the influence of bubble stream and (IV, V) without bubble stream. The red arrow indicates the direction of the rising bubble stream.

the surface tension, and d_c and θ are the basal diameter and contact angle of the bubble on the silicone substrate. The basal diameter of the bubble before detachment is equal to the pinhole diameter on hydrophilic substrates where the contact line remains pinned at the edge of the orifice and will be larger than the pinhole diameter on hydrophobic substrates where dewetting can occur. For example, it has been shown that dewetting around an orifice on a hydrophobic surface with a static contact angle of 100° can lead to bubble basal diameters as large as five times the orifice diameter (Gnyloskurenko, Byakova, Raychenko, & Nakamura, 2003). Using these hydrophilic and hydrophobic bounds on d_c and assuming a 90° contact angle just before detachment, Eq. (8) results in estimates of bubble size in the range 3 mm $< d <$ 5 mm. This estimated value for bubble diameter compares favorably with the observed BC tube diameter of ~3.5 mm.

The alignment of BCM is a consequence of unidirectional force induced by the rising bubble stream. Previous studies suggest that the flow-induced shear force can affect the alignment of the cellulose fibers (Wan et al., 2015). The uniaxial alignment of BCM presented in this study is in good accordance with previous studies and suggests that the shear force generated by the bubble stream during the synthesis can induce the alignment of BCMs. To estimate the magnitude of this shear force, consider the motion of bubbles through the BCM tube after they detach from the silicone substrate. Since the bubbles emerging from the pinhole are comparable in size to tube diameter d_t, they become elongated in the flow direction as they rise through the BCM tube. Elongated bubbles are separated from the tube wall by an annular liquid film of thickness δ in which viscous and gravitational forces balance. Assuming a uniform film thickness (i.e. an idealized long bubble consisting of a cylindrical body connecting the nose and tail), the approximation of unidirectional flow in the liquid film subject to no-slip on the BCM tube wall and zero shear rate at the bubble surface leads to shear stress $\tau = \rho g \delta$ (where ρ is the liquid density) at the tube wall. The film thickness depends on the terminal bubble velocity U_t via conservation of mass, which requires the rate of liquid drainage in the film, $\pi d_t \delta (U_t + 2\rho g \delta^2 / 3\mu)$ (where μ is the liquid viscosity), be equal to the rate at which liquid moves past the bubble, $\pi d_t^2 U_t / 4$. This yields $\delta \sim (3\mu d_t U_t / 4\rho g)^{1/3}$ for the thickness of the annular liquid film, with a corresponding $U_t^{1/3}$ dependence for the wall shear stress. To find the magnitude of this shear force, the terminal velocity of the bubble must be estimated.

The steady rise velocity of a bubble is determined by the balance between buoyancy and drag forces acting on it. Since the bubble surface is shear-free, the annular liquid film contributes very little to the drag force on an elongated bubble. The drag force on the bubble arises mainly from hydrodynamic stresses on its nose and tail sections where inertial and surface tension effects are important. The dimensionless rise velocity $U_t/(gd_t)^{1/2}$ of elongated bubbles becomes nearly independent of the buoyancy Reynolds number ($Re_b = \rho(gd_t^3)^{1/2}/\mu$) for bubbles with $Re_b > 20$(Viana, Pardo, YÁNez, Trallero, & Joseph, 2003). The elongated air bubbles rising in the BCM tube of 3.5 mm diameter are characterized by Re_b on the order of 500, for which the dimensionless bubble speed is about 0.005 (Viana et al., 2003). This leads to an estimated bubble speed of about 1 mm/s and corresponding shear stress on the order of ~1 Pa. Previous studies reported that other bacteria with a diameter of ~1 μm were pulled away from the surface of polymer films by the flow-induced shear stress of ~1 Pa or lower (Lopez-Mila et al., 2018; Nejadnik et al., 2008).

Elongated bubbles rising at about 1 mm/s in a BCM tube of 3.5 mm diameter are characterized by the Weber number ($We = \frac{\rho U_t^2 d_t}{\sigma}$) on the order of 10^{-4}, which means surface tension >> inertia. Numerical simulations have shown that large surface tension effects for such bubbles cause thinning of the liquid film towards the bubble tail to constrict the drainage flow at the bulging rim of the tail before releasing the high-speed liquid stream into the expansion behind the bubble tail (Feng, 2008). This can lead to the formation of recirculating eddies in the wake of the bubble near the tube wall. The resulting shear stress acts to pull

the bacteria upward near the wall while the shear stress in the liquid film pulls down on the cellulose microfibrils. As the cellulose microfibrils are adhered or entangled to each other in the BCM tube and the shear stress pulls the bacteria upward during the cultivation, the extrusion of cellulose microfibrils from bacteria should be downward. Increasing the gas flow rate through the silicone tube beyond 0.25 vvm would not affect the bubble size (see Eq. (8)), but would reduce the time between successive bubble releases. This would reduce the bubble spacing and could cause a change in the flow structure by eliminating the recirculating eddies behind bubbles.

3.3. Parallel packing with added polarity of crystalline cellulose Iα in the BCM tube

The synthesis process of *G. hansenii* preferentially occurs on the non-reducing end of cellulose chains (Koyama et al., 1997). Therefore, the directional synthesis under the bubble stream suggests that crystalline cellulose Iα in the BCM tube is expected to be aligned in a parallel fashion (one direction from reducing end to non-reducing end of cellulose chain). The parallel alignment of crystalline cellulose Iα in the aligned BCM was confirmed through the SFG measurement as a function of azimuth angle.

SFG is a nonlinear optical process that detects non-centrosymmetrically arranged vibrational modes only (Chae et al., 2017; Lambert et al., 2005); thus, it can selectively detect vibrational

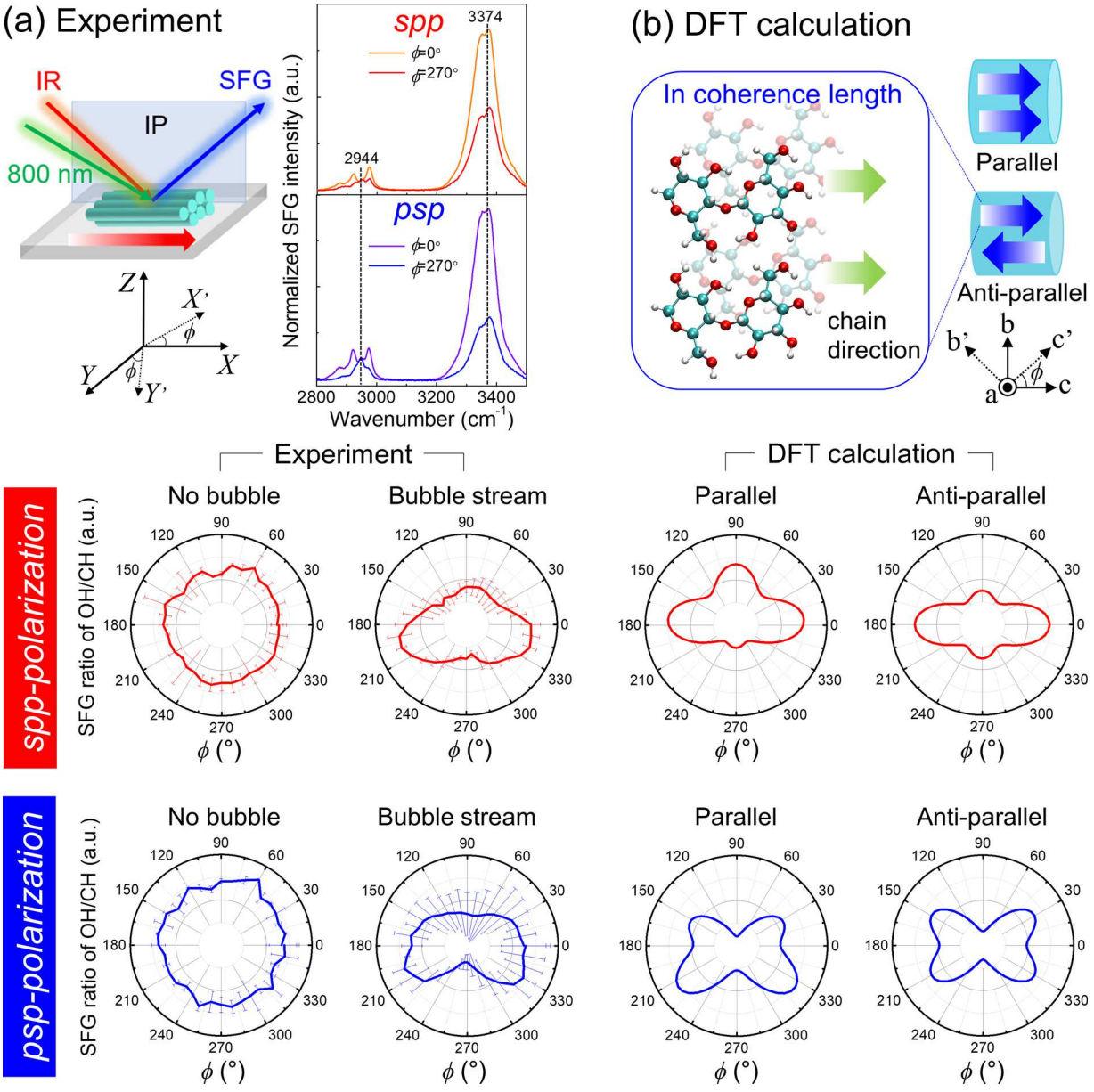

Fig. 3. (a) Schematics with the laboratory coordinates (*X*, *Y*, *Z*) and experimental results of azimuth angle-dependent SFG spectroscopy. The laser incident plane (IP) is in the *Z*-*X* plane, and the parallel alignment of BCM is along the *X*-axis. The *spp*- and *psp* SFG spectra were normalized with the peak intensity at 2944 cm^{-1}. The BCM sample is rotated along the *Z*-axis to induce the variation of ϕ. The SFG peak intensity ratios of OH (3374 cm^{-1}) / CH (2944 cm^{-1}) with *spp*- and *psp*-polarization combinations with and without the bubble-stream were plotted as a function of ϕ. The average and standard deviations of SFG signals at three different locations are displayed. The red arrow in the schematics represents the direction of the bubble stream during cultivation. (b) TD-DFT model with the molecular frame (*a*, *b*, *c*) and calculations of the SFG ratios (OH/CH) of cellulose Iα with parallel and anti-parallel packing. Cellulose Iα crystalline in coherence length is illustrated with blue arrows pointing the same direction of cellulose chains (green arrows).

modes of cellulose Iα with the non-centrosymmetric P1 space group and does not suffer from the interference of amorphous matrices (Barnette et al., 2011; Kim et al., 2013; Lambert et al., 2005). In resonance with vibrational modes, the intensity of SFG (I_{SFG}) can be described as (Lambert et al., 2005; Lee et al., 2014)

$$\frac{I_{SFG}}{I_{IR}I_{VIS}} \propto \left|\chi_{eff}^{(2)}\right|^2 sinc^2\left(\frac{\Delta KL}{2}\right)L^2 \quad (9)$$

where I_{IR} and I_{VIS} are the intensities of IR and visible beams, respectively. $\chi_{eff}^{(2)}$ and $sinc^2\left(\frac{\Delta KL}{2}\right)$ are the effective second-order nonlinear susceptibility and synchronization factor, respectively. The synchronization term depends on the phase mismatch (ΔK) between SFG, visible and IR, and sample size (L), respectively (Lee et al., 2014; Makarem et al., 2019). In previous studies, it was found that the SFG signal intensities of OH stretching modes are sensitive to the packing polarity, whereas those of CH and CH_2 stretching modes are sensitive to the density of crystalline cellulose (Chae et al., 2019; Makarem et al., 2017). Thus, the SFG signal intensity ratio of OH/CH vibrational modes can provide the information of polar ordering of crystalline cellulose within the coherence length ($L_c \approx 2/\Delta K$) (Chae et al., 2019, 2020; Lee CM et al., 2017). The coherence requirement with the phase match of SFG makes the intensity ratio of OH/CH modes also sensitive to the spatial distance between cellulose crystals (Makarem et al., 2017, 2020). Because of multiple parameters affecting the SFG intensity ratio, it is difficult to identify arrangements of crystalline cellulose with a single measurement. Chen et al. resolved this issue through TD-DFT calculations of the full azimuth angle dependence of $\chi_{eff}^{(2)}$, then identified the uniaxial packing of crystalline cellulose (Chen, Lee, Wang, Jensen, & Kim, 2017). Using the same principle, we test and confirm the parallel packing of crystalline cellulose in the bubble stream-induced BCM tube.

Fig. 3a shows the schematics of SFG measurement on the aligned BCM as a function of azimuth angle (ϕ). The azimuth angle of 0° was set to the direction of the rising bubble (red arrow) along the positive *X*-axis in the schematics. The SFG intensity ratio of OH/CH was recorded by rotating every 10° of ϕ along the anti-clockwise direction. Two different polarization combinations were employed – *spp* (*s*: SFG, *p*: 800 nm, *p*: IR) and *psp* polarizations, which are sensitive to chiral species only (Chae et al., 2019; Yan, Fu, Wang, & Liu, 2014). Thus, adventitious organic contaminants at the BCM surface cannot contribute to the detected SFG signal. The spectral intensities were normalized by the CH peak intensity at 2944 cm^{-1} for a comparison purpose. The SFG spectra in both polarization combinations show much higher OH signals (3200–3500 cm^{-1}) than CH signals (2800–3000 cm^{-1}). Our recent theoretical calculations found that the OH/CH intensity ratio larger than 2–3 for the sample with the cellulose volume fraction larger than 10–20 % is the characteristic feature of the parallel packing of crystalline cellulose domains (Makarem et al., 2020). Thus, the SFG spectra shown in Fig. 3a are consistent with the expected feature of the parallel packing. This interpretation is further corroborated through the full azimuth angle dependence analysis of SFG. Fig. 3b shows the simulated cellulose Iα models for TD-DFT calculations of the parallel and anti-parallel cases. The TD-DFT calculations were employed to interpret the experimentally measured SFG signals. In the parallel case of TD-DFT, all cellulose Iα chains are aligned along one direction (from reducing end to non-reducing end). Considering the rotational freedom of BCM along the long axis of fibrils, different rotational angle along the chain axis (c-axis) of cellulose in each coherence domain is considered in the calculation, as shown in Eq. (3).

The TD-DFT calculations predict asymmetric azimuth angle dependences of both *spp* and *psp* SFG polarizations for the parallel packing. In the polar plot, the shape of SFG OH/CH ratio in 0° → 180° region (upward) is different from that in the 180° → 0° region (downward). In the *spp* polarization, three major lobes appear near 0°, 90° and 180° in the polar plot. In *psp* polarization, two bigger lobes appear near 220° and 320°, and two smaller lobes appear near 30° and 150°. On the other hand, symmetric shapes-the same SFG ratios along with the opposite directions of any azimuth angle-appear in both *spp* and *psp* polarizations for the anti-parallel case in TD-DFT calculation. In the anti-parallel case, opposite directions of cellulose Iα chains separated farther than the coherence length are equally added (Baudrier-Raybaut, Haïdar, Kupecek, Lemasson, & Rosencher, 2004); thus, the symmetric shapes are anticipated. In our previous study, the monolayer of crystalline cellulose Iβ with anti-parallel packing showed the similar symmetric shapes in the same measurement (Chae et al., 2020). Randomly arranged BCMs cultivated without the bubbling shows circular shapes in both *spp* and *psp* polarizations because of the isotropic arrangement of crystalline cellulose Iα in the SFG probing area (~80 μm × ~120 μm) (Lee, Kafle, Huang, & Kim, 2016). The asymmetric shapes of azimuth angle-dependent SFG ratio of OH/CH confirm the parallel packing of cellulose Iα in the BCM tube produced with the bubble stream culture method.

The asymmetric azimuth angle dependence is due to asymmetric variations of $\chi_{ijk}^{(2)}$ tensors (SFG polarization induced in the *i*-direction by the electric field of VIS in the *j*-axis and that of IR in the *k*-axis) at different azimuth angles. This phenomenon is explained with the example of TD-DFT calculation for the parallel case in *spp* polarization, as shown in Fig. 4. At $\phi = 0°$ (black in Fig. 4) and 180° (green in Fig. 4), the χ_{YXZ} is the dominant component with the same sign contributing to *spp* polarization in both OH and CH vibrational modes. Its magnitude is the same at $\phi = 0°$ and 180°, which explains the symmetric magnitude along the *X*-axis (0° − 180°) in the polar plot of the azimuth angle-dependence. At $\phi = 90°$ and 270°, χ_{YXX} and χ_{YZZ} are the dominant components and they have the opposite sign for the OH and CH modes. At $\phi = 90°$ (red), the other two contributors, χ_{YXZ} and χ_{YZX}, have the same signs with the dominant χ_{YXX} in the O—H mode whereas they have the opposites signs to the dominant χ_{YZZ} in the C—H mode. At $\phi = 270°$ (blue), χ_{YXZ} and χ_{YZX} have the opposite signs to the dominant χ_{YXX} in the O—H mode whereas they have the same signs to the dominant χ_{YZZ} in C—H mode. Therefore, the calculated SFG ratio of OH/CH in *spp* polarization at $\phi = 90°$ is larger than that at $\phi = 270°$ (Fig. 3b).

Fig. 5 shows the schematics and results of the SHG measurements of the parallel-aligned BCM tube and random BCM film. The aligned BCM tube shows strong SHG responses due to the parallel packing of polar crystalline cellulose Iα. SHG is the frequency doubling phenomenon in nonlinear optics, defined as (Denev et al., 2011)

$$P^{2\omega} = \chi^{(2)}\,(E^{\omega})^2 \quad (10)$$

in Einstein notation, where $P^{2\omega}$, $\chi^{(2)}$ and E^{ω} are nonlinear polarization, second-order susceptibility, and electric field at frequency ω. Similar to SFG, SHG occurs only in the non-centrosymmetric system; thus, it can be a supplementary tool to confirm the non-centrosymmetric packing of BCMs (Denev et al., 2011). As the space group of crystalline cellulose Iα is P1, each crystalline domain can be SHG-active (Cellulose, 2008). At 800 nm probing wavelength, the SHG arises from the anharmonic energy potentials of the electron clouds around the nucleus (Denev et al., 2011). Fig. 5a describes the transmission geometry of SHG measurement on the aligned BCM tube. The incident polarization angle (ψ) of 0° was set for the incident polarization of 800 nm beam along the direction of the rising bubble (red arrow, *X*-axis) in the schematics. The aligned BCM tube shows large incident-polarization-dependence in SHG (Fig. 5b), whereas the control sample cultivated without bubbling exhibit very weak SHG signals and no angle dependence (Fig. 5c; note that the plot is magnified by ×5) for the same thickness of ~20 μm. The aligned BCM tube has crystalline cellulose Iα packed along one direction, which results in the constructive interference when the incident 800 nm beam passes through the sample. On the other hand, when the beam propagates through the randomly arranged BCM, the SHG response is canceled within the coherence length due to the destructive interference.

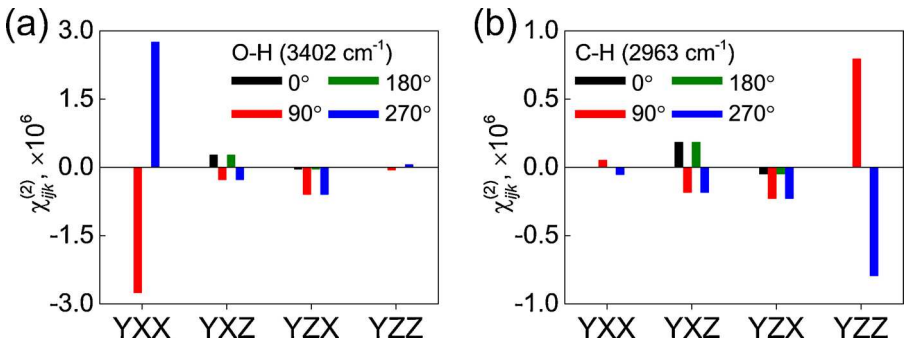

Fig. 4. Azimuth angle (ϕ) dependent $\chi^{(2)}_{ijk}$ tensors (*x*-axes of graphs corresponding to *ijk*), contributing to *spp* polarization SFG signal of cellulose I α with the (200) plane in the *X*-*Y* plane. Frequency at (a) 3402 cm^{-1} and (b) 2963 cm^{-1} for OH and CH modes, respectively.

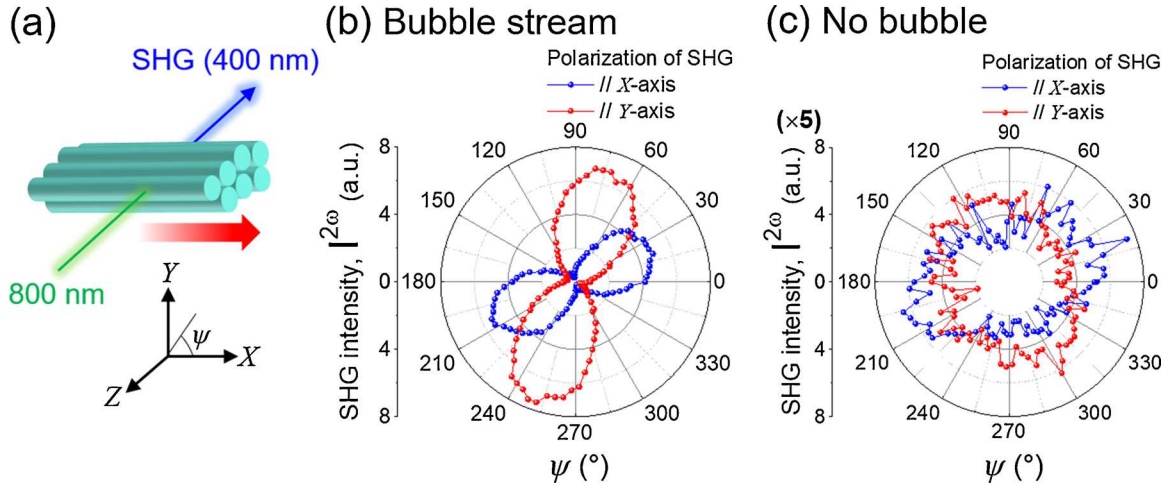

Fig. 5. (a) Schematics of incident polarization angle-dependent SHG measurement on the aligned BCM in a transmission mode. The incident 800 nm beam is aligned along the *Z*-axis, and its polarization is rotated within the *X*-*Y* plane (ψ). The red arrow represents the direction of the bubble stream during cultivation. SHG intensity of (b) aligned BCM with bubble-stream and (c) random BCM without bubbling as a function of ψ. The polarization of SHG is fixed along the *X*-axis (blue dots) or *Y*-axis (red dots). The thickness of both samples is ~20 μm.

4. Conclusion

Polar alignment of BCMs with the parallel packing of cellulose Iα crystalline domains was achieved in this study. As the wet-air bubble stream supplied oxygen to *G. hansenii* bacteria in the culture medium, the BCM tube was formed along the bubble path with the tethering process. Also, the bubble stream continuously applied the shear stress on the inner side of the BCM tube in the order of ~1 Pa (mathematical estimation) such that newly synthesized BCMs on the tube were aligned in a parallel fashion. The azimuth-angle dependent SFG analysis of the BCM tube confirmed that the cellulose Iα crystals are aligned along one direction, from reducing end to non-reducing end of cellulose chains. Due to the parallel alignment, net dipoles of cellulose crystalline domains were added on a macroscopic scale and the strong SHG signal was generated. The method demonstrated in this study is expected to provide opportunities for studying material properties unique to the low symmetry of crystalline biopolymers which require the polar alignment of such domains.

CRediT authorship contribution statement

Inseok Chae: Conceptualization, Methodology, Validation, Formal analysis, Investigation, Writing - original draft. **Syed M.Q. Bokhari:** Conceptualization, Methodology, Formal analysis, Resources, Visualization, Writing - original draft. **Xing Chen:** Software, Formal analysis. **Rui Zu:** Investigation. **Ke Liu:** Conceptualization, Methodology. **Ali Borhan:** Formal analysis, Writing - review & editing. **Venkatraman Gopalan:** Supervision. **Jeffrey M. Catchmark:** Conceptualization, Writing - review & editing, Supervision. **Seong H. Kim:** Conceptualization, Validation, Formal analysis, Writing - review & editing, Supervision, Project administration, Funding acquisition.

Acknowledgments

This work was supported by the iSuperSEED program of the Penn State Materials Research Science & Engineering Center (MRSEC), funded by the National Science Foundation (NSF, Grant No. DMR-1420620). The cultivation of bacterial cellulose was partially supported by the United States Department of Agriculture, National Institute of Food and Agriculture Federal Appropriations under the project of Pennsylvania Agricultural Experiment Station, 4602 (Accession No. 1009850). The SHG work was supported by another NSF program (Grant No. DMR-1807768).

Appendix A. Supplementary data

Supplementary material related to this article can be found, in the online version, at doi:https://doi.org/10.1016/j.carbpol.2020.117328.

References

Arcot, L. R., Lundahl, M., Rojas, O. J., & Laine, J. (2014). Asymmetric cellulose nanocrystals: thiolation of reducing end groups via NHS–EDC coupling. *Cellulose, 21*(6), 4209–4218.

Barhoumi Meddeb, A., Chae, I., Han, A., Kim, S. H., & Ounaies, Z. (2020). Magnetic field effects on cellulose nanocrystal ordering in a non-aqueous solvent. *Cellulose*.

Barnette, A. L., Bradley, L. C., Veres, B. D., Schreiner, E. P., Park, Y. B., Park, J., & Kim, S. H. (2011). Selective detection of crystalline cellulose in plant cell walls with Sum-Frequency-Generation (SFG) vibration spectroscopy. *Biomacromolecules, 12*(7), 2434–2439.

Baudrier-Raybaut, M., Haïdar, R., Kupecek, P., Lemasson, P., & Rosencher, E. (2004). Random quasi-phase-matching in bulk polycrystalline isotropic nonlinear materials. *Nature, 432*(7015), 374–376.

Bodin, A., Bäckdahl, H., Fink, H., Gustafsson, L., Risberg, B., & Gatenholm, P. (2007). Influence of cultivation conditions on mechanical and morphological properties of bacterial cellulose tubes. *Biotechnology and Bioengineering, 97*(2), 425–434.

Bordel, D., Putaux, J.-L., & Heux, L. (2006). Orientation of native cellulose in an electric field. *Langmuir, 22*(11), 4899–4901.

Cellulose. (2008). *Crystalline cellulose and derivatives: Characterization and structures* (pp. 101–174). Berlin, Heidelberg: Springer Berlin Heidelberg.

Chae, I., Ahmed, S., Atitallah, H. B., Luo, J., Wang, Q., Ounaies, Z., … Kim, S. H. (2017). Vibrational sum Frequency Generation (SFG) analysis of ferroelectric response of PVDF-based copolymer and terpolymer. *Macromolecules, 50*(7), 2838–2844.

Chae, I., Jeong, C. K., Ounaies, Z., & Kim, S. H. (2018). Review on electromechanical coupling properties of biomaterials. *ACS Applied Bio Materials, 1*(4), 936–953.

Chae, I., Ngo, D., Makarem, M., Ounaies, Z., & Kim, S. H. (2019). Compression-induced topographic corrugation of air/surfactant/water interface: Effect of nanoparticles adsorbed beneath the interface. *The Journal of Physical Chemistry C, 123*(42), 25628–25634.

Chae, I., Ngo, D., Chen, Z., Kwansa, A. L., Chen, X., Meddeb, A. B., & Kim, S. H. (2020). Anisotropic optical and frictional properties of Langmuir–Blodgett film consisting of uniaxially-aligned rod-shaped cellulose nanocrystals. *Advanced Materials Interfaces*, Article 1902169. n/a(n/a).

Chang, H., Chien, A.-T., Liu, H. C., Wang, P.-H., Newcomb, B. A., & Kumar, S. (2015). Gel spinning of polyacrylonitrile/cellulose nanocrystal composite fibers. *ACS Biomaterials Science & Engineering, 1*(7), 610–616.

Chen, X., Lee, C. M., Wang, H.-F., Jensen, L., & Kim, S. H. (2017). Experimental and theoretical study of azimuth angle and polarization dependences of sum-frequency-generation vibrational spectral features of uniaxially aligned cellulose crystals. *The Journal of Physical Chemistry C, 121*(34), 18876–18886.

Chung, W.-J., Oh, J.-W., Kwak, K., Lee, B. Y., Meyer, J., Wang, E., & Lee, S.-W. (2011). Biomimetic self-templating supramolecular structures. *Nature, 478*, 364.

Cranston, E. D., & Gray, D. G. (2008). Birefringence in spin-coated films containing cellulose nanocrystals. *Colloids and Surfaces A, Physicochemical and Engineering Aspects, 325*(1), 44–51.

Csoka, L., Hoeger, I. C., Peralta, P., Peszlen, I., & Rojas, O. J. (2011). Dielectrophoresis of cellulose nanocrystals and alignment in ultrathin films by electric field-assisted shear assembly. *Journal of Colloid and Interface Science, 363*(1), 206–212.

De France, K. J., Yager, K. G., Hoare, T., & Cranston, E. D. (2016). Cooperative ordering and kinetics of cellulose nanocrystal alignment in a magnetic field. *Langmuir, 32*(30), 7564–7571.

Denev, S. A., Lummen, T. T. A., Barnes, E., Kumar, A., & Gopalan, V. (2011). Probing ferroelectrics using optical second harmonic generation. *Journal of the American Ceramic Society, 94*(9), 2699–2727.

Diddens, I., Murphy, B., Krisch, M., & Müller, M. (2008). Anisotropic elastic properties of cellulose measured using inelastic X-ray scattering. *Macromolecules, 41*(24), 9755–9759.

Dumanli, A. G., Kamita, G., Landman, J., van der Kooij, H., Glover, B. J., Baumberg, J. J., & Vignolini, S. (2014). Controlled, bio-inspired self-assembly of cellulose-based chiral reflectors. *Advanced Optical Materials, 2*(7), 646–650.

Feng, J. Q. (2008). Buoyancy-driven motion of a gas bubble through viscous liquid in a round tube. *Journal of Fluid Mechanics, 609*, 377–410.

Frka-Petesic, B., Jean, B., & Heux, L. (2014). First experimental evidence of a giant permanent electric-dipole moment in cellulose nanocrystals. *EPL (Europhysics Letters), 107*(2), 28006.

Frka-Petesic, B., Sugiyama, J., Kimura, S., Chanzy, H., & Maret, G. (2015). Negative diamagnetic anisotropy and birefringence of cellulose nanocrystals. *Macromolecules, 48*(24), 8844–8857.

García, Y., Ruiz-Blanco, Y. B., Marrero-Ponce, Y., & Sotomayor-Torres, C. M. (2016). Orthotropic piezoelectricity in 2D nanocellulose. *Scientific Reports, 6*(1), 34616.

Gindl, W., Emsenhuber, G., Maier, G., & Keckes, J. (2009). Cellulose in never-dried gel oriented by an AC electric field. *Biomacromolecules, 10*(5), 1315–1318.

Gnyloskurenko, S. V., Byakova, A. V., Raychenko, O. I., & Nakamura, T. (2003). Influence of wetting conditions on bubble formation at orifice in an inviscid liquid. Transformation of bubble shape and size. *Colloids and Surfaces A, Physicochemical and Engineering Aspects, 218*(1), 73–87.

Halasyamani, P. S., & Poeppelmeier, K. R. (1998). Noncentrosymmetric oxides. *Chemistry of Materials, 10*(10), 2753–2769.

Hestrin, S., & Schramm, M. (1954). Synthesis of cellulose by Acetobacter xylinum. 2. Preparation of freeze-dried cells capable of polymerizing glucose to cellulose. *The Biochemical Journal, 58*(2), 345–352.

Hieta, K., Kuga, S., & Usuda, M. (1984). Electron staining of reducing ends evidences a parallel-chain structure in Valonia cellulose. *Biopolymers, 23*(10), 1807–1810.

Hoeger, I., Rojas, O. J., Efimenko, K., Velev, O. D., & Kelley, S. S. (2011). Ultrathin film coatings of aligned cellulose nanocrystals from a convective-shear assembly system and their surface mechanical properties. *Soft Matter, 7*(5), 1957–1967.

Huang, Y.-F., Wang, Y.-F., & Yan, X.-P. (2010). Amine-functionalized magnetic nanoparticles for rapid capture and removal of bacterial pathogens. *Environmental Science & Technology, 44*(20), 7908–7913.

Iyer, K. R. K., Neelakantan, P., & Radhakrishnan, T. (1968). Birefringence of native cellulosic fibers. I. Untreated cotton and ramie. *Journal of Polymer Science Part A-2 Polymer Physics, 6*(10), 1747–1758.

Kim, N.-H., Imai, T., Wada, M., & Sugiyama, J. (2006). Molecular directionality in cellulose polymorphs. *Biomacromolecules, 7*(1), 274–280.

Kim, S. H., Lee, C. M., & Kafle, K. (2013). Characterization of crystalline cellulose in biomass: Basic principles, applications, and limitations of XRD, NMR, IR, Raman, and SFG. *The Korean Journal of Chemical Engineering, 30*(12), 2127–2141.

Kondo, T., Nojiri, M., Hishikawa, Y., Togawa, E., Romanovicz, D., & Brown, R. M. (2002). Biodirected epitaxial nanodeposition of polymers on oriented macromolecular templates. *Proceedings of the National Academy of Sciences, 99*(22), 14008–14013.

Koyama, M., Helbert, W., Imai, T., Sugiyama, J., & Henrissat, B. (1997). Parallel-up structure evidences the molecular directionality during biosynthesis of bacterial cellulose. *Proceedings of the National Academy of Sciences, 94*(17), 9091–9095.

Lagerwall, J. P. F., Schütz, C., Salajkova, M., Noh, J., Hyun Park, J., Scalia, G., & Bergström, L. (2014). Cellulose nanocrystal-based materials: From liquid crystal self-assembly and glass formation to multifunctional thin films. *NPG Asia Materials, 6*, e80.

Lai-Kee-Him, J., Chanzy, H., Müller, M., Putaux, J.-L., Imai, T., & Bulone, V. (2002). In vitro versus in vivocellulose microfibrils from plant primary wall synthases: structural differences. *The Journal of Biological Chemistry, 277*(40), 36931–36939.

Lambert, A. G., Davies, P. B., & Neivandt, D. J. (2005). Implementing the theory of sum frequency generation vibrational spectroscopy: A tutorial review. *Applied Spectroscopy Reviews, 40*(2), 103–145.

Lee, C. M., Kafle, K., Park, Y. B., & Kim, S. H. (2014). Probing crystal structure and mesoscale assembly of cellulose microfibrils in plant cell walls, tunicate tests, and bacterial films using vibrational sum frequency generation (SFG) spectroscopy. *Journal of the Chemical Society Faraday Transactions, 16*(22), 10844–10853.

Lee, C. M., Gu, J., Kafle, K., Catchmark, J., & Kim, S. H. (2015). Cellulose produced by Gluconacetobacter xylinus strains ATCC 53524 and ATCC 23768: Pellicle formation, post-synthesis aggregation and fiber density. *Carbohydrate Polymers, 133*, 270–276.

Lee, C. M., Kafle, K., Huang, S., & Kim, S. H. (2016). Multimodal broadband vibrational sum frequency generation (MM-BB-V-SFG) spectrometer and microscope. *The Journal of Physical Chemistry B, 120*(1), 102–116.

Lee, C. M., Chen, X., Weiss, P. A., Jensen, L., & Kim, S. H. (2017). Quantum mechanical calculations of vibrational sum-frequency-Generation (SFG) spectra of cellulose: Dependence of the CH and OH peak intensity on the polarity of cellulose chains within the SFG coherence domain. *The Journal of Physical Chemistry Letters, 8*(1), 55–60.

Lee, J. H., Fan, B., Samdin, T. D., Monteiro, D. A., Desai, M. S., Scheideler, O., & Lee, S.-W. (2017). Phage-based structural color sensors and their pattern recognition sensing system. *ACS Nano, 11*(4), 3632–3641.

Liu, K., & Catchmark, J. M. (2019). Bacterial cellulose/hyaluronic acid nanocomposites production through co-culturing Gluconacetobacter hansenii and Lactococcus lactis in a two-vessel circulating system. *Bioresource Technology, 290*, Article 121715.

Lokanathan, A. R., Nykänen, A., Seitsonen, J., Johansson, L.-S., Campbell, J., Rojas, O. J., & Laine, J. (2013). Cilia-mimetic hairy surfaces based on end-immobilized nanocellulose colloidal rods. *Biomacromolecules, 14*(8), 2807–2813.

Lopez-Mila, B., Alves, P., Riedel, T., Dittrich, B., Mergulhão, F., & Rodriguez-Emmenegger, C. (2018). Effect of shear stress on the reduction of bacterial adhesion to antifouling polymers. *Bioinspiration & Biomimetics, 13*(6), Article 065001.

Makarem, M., Sawada, D., O'Neill, H. M., Lee, C. M., Kafle, K., Park, Y. B., & Kim, S. H. (2017). Dependence of sum frequency generation (SFG) spectral features on the mesoscale arrangement of SFG-active crystalline domains interspersed in SFG-inactive matrix: A case study with cellulose in uniaxially aligned control samples and alkali-treated secondary cell walls of plants. *The Journal of Physical Chemistry C, 121*(18), 10249–10257.

Makarem, M., Lee, C. M., Kafle, K., Huang, S., Chae, I., Yang, H., & Kim, S. H. (2019). Probing cellulose structures with vibrational spectroscopy. *Cellulose, 26*(1), 35–79.

Makarem, M., Nishiyama, Y., Xin, X., Durachko, D., Gu, Y., Cosgrove, D. J., … Kim, S. H. (2020). Distinguishing mesoscale polar order (Unidirectional vs. Bidirectional) of cellulose microfibrils in plant cell walls using sum frequency generation spectroscopy. *The Journal of Physical Chemistry B, 124*(37), 8071–8071.

Morgan, J. L. W., Strumillo, J., & Zimmer, J. (2013). Crystallographic snapshot of cellulose synthesis and membrane translocation. *Nature, 493*(7431), 181–186.

Morgan, J. L. W., McNamara, J. T., & Zimmer, J. (2014). Mechanism of activation of bacterial cellulose synthase by cyclic di-GMP. *Nature Structural & Molecular Biology, 21*(5), 489–496.

Morgan, J. L. W., McNamara, J. T., Fischer, M., Rich, J., Chen, H.-M., Withers, S. G., … Zimmer, J. (2016). Observing cellulose biosynthesis and membrane translocation in crystallo. *Nature, 531*(7594), 329–334.

Nejadnik, M. R., van der Mei, H. C., Busscher, H. J., & Norde, W. (2008). Determination of the shear force at the balance between bacterial attachment and detachment in weak-adherence systems, using a flow displacement chamber. *Applied and Environmental Microbiology, 74*(3), 916–919.

Ogawa, Y., Kobayashi, K., Kimura, S., Nishiyama, Y., Wada, M., & Kuga, S. (2013). X-ray texture analysis indicates downward spinning of chitin microfibrils in tubeworm tube. *Journal of Structural Biology, 184*(2), 212–216.

Putra, A., Kakugo, A., Furukawa, H., Gong, J. P., & Osada, Y. (2008). Tubular bacterial cellulose gel with oriented fibrils on the curved surface. *Polymer, 49*(7), 1885–1891.

Rajala, S., Siponkoski, T., Sarlin, E., Mettänen, M., Vuoriluoto, M., Pammo, A., & Tuukkanen, S. (2016). Cellulose nanofibril film as a piezoelectric sensor material. *ACS Applied Materials & Interfaces, 8*(24), 15607–15614.

Ramakrishnan, S., Kumar, R., & Kuloor, N. R. (1969). Studies in bubble formation—I bubble formation under constant flow conditions. *Chemical Engineering Science, 24*(4), 731–747.

Sano, M. B., Rojas, A. D., Gatenholm, P., & Davalos, R. V. (2010). Electromagnetically controlled biological assembly of aligned bacterial cellulose nanofibers. *Annals of Biomedical Engineering, 38*(8), 2475–2484.

Shoulders, M. D., & Raines, R. T. (2009). Collagen structure and stability. *Annual Review of Biochemistry, 78*, 929–958.

Trolier-McKinstry, S. (2008). Crystal chemistry of piezoelectric materials. In A. Safari, & E. K. Akdoğan (Eds.), *Piezoelectric and acoustic materials for transducer applications* (pp. 39–56). Boston, MA: Springer US.

Valiev, M., Bylaska, E. J., Govind, N., Kowalski, K., Straatsma, T. P., Van Dam, H. J. J., … de Jong, W. A. (2010). NWChem: A comprehensive and scalable open-source solution for large scale molecular simulations. *Computer Physics Communications, 181*(9), 1477–1489.

Viana, F., Pardo, R., YÁNez, R., Trallero, J. L., & Joseph, D. D. (2003). Universal correlation for the rise velocity of long gas bubbles in round pipes. *Journal of Fluid Mechanics, 494*, 379–398.

Wan, Y., Hu, D., Xiong, G., Li, D., Guo, R., & Luo, H. (2015). Directional fluid induced self-assembly of oriented bacterial cellulose nanofibers for potential biomimetic tissue engineering scaffolds. *Materials Chemistry and Physics, 149-150*, 7–11.

Yan, E. C. Y., Fu, L., Wang, Z., & Liu, W. (2014). Biological macromolecules at interfaces probed by chiral vibrational sum frequency generation spectroscopy. *Chemical Reviews, 114*(17), 8471–8498.

Yao, K., Meng, Q., Bulone, V., & Zhou, Q. (2017). Flexible and responsive chiral nematic cellulose nanocrystal/poly(ethylene glycol) composite films with uniform and tunable structural color. *Advanced Materials, 29*(28), Article 1701323.

Zang, S., Sun, Z., Liu, K., Wang, G., Zhang, R., Liu, B., … Yang, G. (2014). Ordered manufactured bacterial cellulose as biomaterial of tissue engineering. *Materials Letters, 128*, 314–318.